ARTICLE IN PRESS

Nature Communications

https://doi.org/10.1038/s41467-026-70998-9

Article in Press

Zipper-inspired molecular polarity strategy enabling robust adhesive hydroplastics as sustainable plastic substitutes

Received: 26 October 2025

Accepted: 11 March 2026

Cite this article as: Chen, G., Huang, C., Dong, Y. *et al.* Zipper-inspired molecular polarity strategy enabling robust adhesive hydroplastics as sustainable plastic substitutes. *Nat Commun* (2026). https://doi.org/10.1038/s41467-026-70998-9

Guozhuo Chen, Chengling Huang, Yanjuan Dong, Yi Zheng, Yi Chen, Kam Chiu Tam & Hou-Yong Yu

We are providing an unedited version of this manuscript to give early access to its findings. Before final publication, the manuscript will undergo further editing. Please note there may be errors present which affect the content, and all legal disclaimers apply.

If this paper is publishing under a Transparent Peer Review model then Peer Review reports will publish with the final article.

ARTICLE IN PRESS

© The Author(s) 2026. **Open Access** This article is licensed under a Creative Commons Attribution-NonCommercial-NoDerivatives 4.0 International License, which permits any non-commercial use, sharing, distribution and reproduction in any medium or format, as long as you give appropriate credit to the original author(s) and the source, provide a link to the Creative Commons licence, and indicate if you modified the licensed material. You do not have permission under this licence to share adapted material derived from this article or parts of it. The images or other third party material in this article are included in the article's Creative Commons licence, unless indicated otherwise in a credit line to the material. If material is not included in the article's Creative Commons licence and your intended use is not permitted by statutory regulation or exceeds the permitted use, you will need to obtain permission directly from the copyright holder. To view a copy of this licence, visit http://creativecommons.org/licenses/by-nc-nd/4.0/.

Zipper-inspired molecular polarity strategy enabling robust adhesive hydroplastics as sustainable plastic substitutes

Guozhuo Chen [1], *Chengling Huang* [1], *Yanjuan Dong* [1], *Yi Zheng* [1], *Yi Chen* [1], *Kam Chiu Tam* [2], *Hou-Yong Yu* [1] *

[1] State Key Laboratory of Bio-based Fiber Materials, Zhejiang Sci-Tech University, Xiasha Higher Education Park Avenue 2 No. 928, Hangzhou 310018, China

[2] Department of Chemical Engineering, University of Waterloo, 200 University Avenue West, Waterloo, Ontario, Canada N2L 3G1.

---

*Corresponding author:

E–mail address: phdyu@zstu.edu.cn (H.Y. Yu)

Abstract

Hydroplastics with water-plasticizing effects and programmability are highly desired yet challenges arise from assembling renewable cellulose into hydroplastics with reversible adhesion and enhanced mechanical performance through water-enhanced effects. Here, inspired by zippers, the issue that water molecules are difficult to enhance the comprehensive performances of hydroplastics is addressed by regulating molecular-scale polarity using thioctic acid (TA), combined with reconfigured molecular network under imbalanced polarity environment created by water. This approach enables the fabrication of transparent cellulose hydroplastics (91%) with mechanical performance that can be enhanced to 203 MPa under hydration-dehydration cycles, surpass most cellulose hydroplastics. Moreover, unlike conventional cellulose hydroplastics, the hydroplastic exhibits excellent water-induced reversible adhesion (up to 37 MPa) and rapid programmability (5 minutes). These unique performance advantages open a unique avenue for cellulose to prepare high-performance multifunctional hydroplastics from top-down, dedicated to replacing traditional plastics and reducing the consumption of petrochemical resources.

Introduction

Throughout the decades, human society and the natural environment have suffered from these two world-class problems: energy scarcity and “white pollution”. Production of traditional petroleum-based plastics has exceeded 390.7 million tons per year, of which only 15 percent is recycled, posing a serious environmental threat[1-4]. In contrast, cellulose, the most abundant and renewable biopolymer, can be produced at a rate of up to 750 billion tons per year[5], which is about 2,000 times the amount of plastic produced. Cellulose is considered an ideal alternative to petroleum-based plastics because of its biocompatibility, thermal stability and degradability[6-8]. The molecular structure of traditional cellulose plastics is rich in hydroxyl groups, allowing hydrogen bond-driven assembly[9]. However, their inherent crystallinity and refractoriness prevent them from having excellent mechanical and deformation processing performance like traditional thermoplastics or thermosets, making it difficult to broaden them to other areas of application[6,10-13].

Recent strategies have been proposed to overcome the intrinsic limitations of cellulosic plastics by incorporating plasticizers or functional modifiers to disrupt the dense hydrogen-bonding network, thereby enabling heat-sealability or water-induced shape programmability[14-17]. Although these methods have achieved a certain degree of improvements in mechanical performance (typically <120 MPa) and shape programmability, they often suffer from high energy consumption (e.g., thermal processing) or restricted programming performance that rely on curvature-based reshaping during hydration-dehydration cycles[18,19]. As a result, these cellulose plastic still fall short of rivaling conventional thermoplastics in terms of integrated performance. More critically, the majority of cellulose hydroplastic primarily rely on reversible hydrogen bonding and treat water as a plasticizer（a medium for swelling and softening）while largely neglecting the potential of dynamic covalent bonds, which offer greater stability and strength[18,20,21].

Unfortunately, the role of water in these hydroplastics remains limited to a macroscopic (swelling–softening–shaping) process, without leveraging its molecular-level capacity to induce network reconfiguration, such as polymer chain rearrangement or crosslink regeneration during hydration-dehydration cycles[18,22]. Therefore, there is urgent to develop strategy that simultaneously preserve water's plasticizing effect and its enhancement effects, enabling the fabrication of high-performance regenerated cellulosic hydroplasitcs.[20,21].

Conventional cellulose hydroplastic absorb water and retain large amounts of bound water, which results in pronounced swelling behavior[23]. Cellulose-water interactions are influenced by the structural network of cellulose molecules[20]. Cellulose chains contain alternating polar (–C–OH) and non-polar (–CH_2) moieties[24]. Due to strong polarity of water molecular, its interactions follow the principles: dipole–dipole attraction (Keesom effect) [25]. Hydrogen bond network in cellulose can be disrupted by introducing highly polar groups and non-polar groups. Changes in polar environments (hydration to dehydration) drive the disruption of molecular network balance. Severe imbalance prompts molecular chains to rearrange and reassemble to achieve a distinctive balanced state, thereby enabling hydroplasitcs enhancement effects. However, exploration of such water-induced enhancement mechanisms is still in its infancy, and current strategies have yet to meet the structural and performance requirements for robust and multifunctional cellulosic plastics.

A zipper is tight when closed, loose when open. Herein, to address the challenges in using water as a enhancing agent and the construction of high-strength cellulose hydroplastics, we propose a zipper-inspired strategy to introduce highly polar groups (carboxyl group, -COOH) and dynamic covalent bonds

(S-S) to build a polar gradient network, enabling a plasticization pathway and conferring water's enhancement effect in hydroplastics. The internal network is reconfigured and re-crosslinked under imbalanced polarity environment created by water. Consequently, ultra-strong cellulose hydroplastics (CCMA) with exciting properties such as high mechanical strength (203 MPa), high modulus (8 Gpa), and reversible adhesion (37 MPa) are obtained under hydration-dehydration cycles. This work is expected to deepen the understanding of the mechanism of cellulose-water interactions at the molecular scale and provide a promising polarity gradient strategy for constructing cellulosic hydroplastics with high performance, moving closer to the goal of reducing reliance on nondegradable petroleum-based plastics.

Results and discussion

Design strategy of polarity-driven CCMA hydroplastics.

In order to achieve cellulose hydroplastics with ultra-strong mechanical performance and adhesive performance, we develope unique molecular design strategy. Thermally induced ring-opening polymerization of the TA dithiopentane ring, which undergoes dynamic S-S bonding reorganization to generate a linear chain[26,27], is utilized, which is then grafted onto a cellulose precursor (CCM, which is cellulose grafted with cinnamon groups) (Fig. 1a-b). The resulting CCMA hydroplastics could be prepared by a scalable solution casting process (Supplementary Fig.1), yielding highly transparent and flexible hydroplastics (Fig. 1c). A smooth and dense lamellar cross-section is observed by scanning electron microscopy (SEM) (Fig. 1d and Supplementary Fig.2). In addition, EDS and energy spectroscopy analysis (FTIR and NMR) and *XPS* confirmed that TA is covalently integrated into the CCMA hydroplastics' network (Supplementary Fig.3-6). Crucially, the FTIR spectra revealed a hydrogen bonding fraction (F_{H-}

$_{OH}$) of 0.69 for CCMA-2 (Supplementary Fig.7-8), highlighting the role of TA in the construction of a dynamic and dense network. Notably, thermal analysis (Supplementary Fig.9-10) further confirmed the stability of CCMA hydroplastics, whose decomposition products are mainly H_2O, CO_2 and C=O fragments. The gas release properties are abundant and the complex decomposition behavior of CCMA hydroplastics suggest a more unique functionality[28].

At the molecular level (Fig. 1e-f), the introduction of TA molecular forms a network (polarity gradient network) containing multiple polar groups such as hydroxyl group of cellulose, -COOH of TA and water molecules. In dipole–dipole attraction (Keesom effect), water molecules interact with highly polar regions such as carboxyl groups, inducing network changes during the hydration-dehydration cycle (Fig. 1g).

Therefore, we achieved the enhancement effect of water molecules on molecular network by utilizing a zipper-inspired design strategy, thereby realizing unique performance (Fig. 1h). Specifically, water acts as a key by opening and softening molecular networks for plasticization. Moreover, water rearranges the molecular network, transforming it into highly ordered, and stable state during dehydration, driven by imbalanced polarity environment. The mechanical performance of CCMA hydroplastics can be strengthened through molecular network rearrangement, as well as adhesion and shape programming (Fig. 1i). Besides, CCMA hydroplastics have more potential for sustainable plastics substitution than other hydroplastics (Fig. 1j and Supplementary Table 1).

Water induced plasticizing and dynamic hydrogen bond evolution

To elucidate the plasticizing process of water molecules on molecular networks, we conducted further research. The dipole moments of different molecules reveal the polarity gradient within the CCMA network (Fig. 2a): cellulose molecules (cellobiose, 5.2 D), CCM molecules (3.9 D), TA (3.6 D), and water (2.0 D). Moreover, surface zeta potential of CCMA hydroplastics exhibit negative value (Fig. 2b), attributed to the deprotonation of terminal carboxyl groups on the TA chain. This phenomenon confirms that TA groups readily interact with water environments. Additionally, the significant increase in the water contact angle of CCMA hydroplastics (Supplementary Fig.11 from 66.5° to 94°) is attributed to the exposure of hydrophobic alkyl chains (TA) on the surface. Moreover, the decrease in the dynamic water contact angle of CCMA-3 indicates that different polarity between -COOH and water molecules exposes the terminal hydrophilic -COOH groups to the water environment, thereby initiating the hydration and plasticization process (Fig. 2c).

To elucidate the dynamic evolution of hydrogen bonds between water and the CCMA network, we conducted further tests. The molecular model of the hydrated system (Supplementary Fig.12) shows that water molecules interact with hydroxyl group (-OH, cellulose) and carboxyl groups (-COOH in TA). According to the ESP analysis of cellulose and TA (Supplementary Fig.13), the oxygen atoms in the molecule are more likely to accept protons to form intermolecular interactions[29]. Radial distribution function (RDF) analysis (Fig. 2d) quantified the probability densities of aqueous oxygen atoms around various oxygen-containing groups. The results show that carboxyl oxygen atoms (-OH in C=O and COOH) have higher hydration peaks and shorter interaction distances compared to –OH (cellulose), suggesting stronger and more frequent hydrogen bond formation with water.

To further visualize the spatial characteristics of these interactions, we employed independent gradient model (IGMH) based on Hirshfeld assignments, which (From Multiwfn) highlights weak non-covalent interactions[30,31] (Fig. 2e and Supplementary Fig.14). The green isosurfaces clearly indicate strong localized hydrogen bonding between water and carboxyl group, while the interactions with the hydroxyl group appear more diffuse and weaker. Moreover, the binding energy under solvation (Fig. 2f) confirms that the hydrogen bond formed between water molecules and carboxyl groups is significantly stronger than that formed with hydroxyl groups[23]. Consequently, water molecules will shift to bond with hydroxyl groups once the carboxyl sites are occupied. Remarkably, the bond between two carboxyl groups is less than the bond energy between a carboxyl group and water, suggesting that water can transcend the intra-network hydrogen bonding and thus reconfigure the molecular network.

Moreover, we performed molecular orbital analysis (Fig. 2g). Water primarily functions as an electron donor (hydrogen bond acceptor, HOMO: -6.7 eV) within this network. Comparing electron acceptor capabilities reveals that the lowest unoccupied molecular orbital (LUMO) energy of TA (-1.9 eV) is significantly lower than that of cellulose (-1.0 eV) (Supplementary Table 2)[32]. According to molecular orbital theory, a smaller energy gap (ΔE) between the donor's highest occupied molecular orbital (HOMO) and the acceptor's LUMO indicates stronger orbital mixing and interaction. The energy gap between TA and water interactions (ΔE = 4.8 eV) is significantly smaller than that between cellulose and water interactions (ΔE = 5.7 eV). Moreover, the LUMO electron density of TA is highly localized at the carboxyl (COOH) head group. This confirms that water molecules preferentially hydrate the carboxyl group of TA under the guidance of electrons.

Further, the IR spectra highlights the hydrogen bonding fraction ($F_{H\text{-}CO}$) that increases with TA content, confirming the formation of a strong intermolecular network (Supplementary Fig.15-16). The areas of the two sets of carboxylate subpeaks of CCMA hydroplastic are compared before and after dehydration (Fig. 2h and Supplementary Fig.17). The results indicate that the dehydrated CCMA hydroplastics release more COOH groups to participate in the rearrangement and relaxation (remodeling) of polymer chains, showing competitive hydrogen bonding interactions. Experimentally, time-dependent ATR-IR spectra are recorded at 25°C during the drying process of CCMA hydroplastics to assess the internal molecule-based water induction mechanism (Supplementary Fig.18). 2D correlation spectroscopy (2D-COS is generated from time-dependent attenuated total reflectance infrared spectra) can provide more insight into the evolutionary sequence of hydrogen bonding during dehydration [33-35] (Fig. 2i). For clarity, all these spectral bands and their associated attributions [18] are listed in Supplementary Table 3. The asynchronous spectra identified subtle bands corresponding to the C=O [36] and O-H[37] groups in different states, suggesting that the dimeric hydrogen bonding between TA chains is finally stabilized during water evaporation. According to Noda's rule [38], the sequential events of specific chemical groups during dynamic dehydration can be determined as follows: 3230 → 3560 → 3446 → 1741 → 1752 → 1703 cm^{-1}, i.e., O6-H6......O3 inter-chain → free OH groups → O2-H2 ......O6 intra-chain → C=O (hydrogen bonding with water) → C=O (free) → C=O (dimerization hydrogen bonding). Moreover, this sequential pattern aligns with the previously observed polarity gradient, thereby further demonstrating the presence of the polarity gradient.

In addition, the diffusion coefficient also indicates that the hydrophobic alkyl segments (TA) in CCMA hydroplastics exert a certain hindrance effect on water molecules (Supplementary Fig.19). Hence,

Fig. 2j summarizes the dynamic evolution mechanism in the zipper model. Water molecules are selectively attracted to highly polar COOH sites when exposed to water (hydration process). Competition for these sites induces hydrogen bonding competition, disrupting existing hydrogen bonds and plasticizing the molecular network. Furthermore, water molecules detach from cellulose hydroxyl sites (-OH) and subsequently from TA carboxyl groups (-COOH) during dehydration. CCMA hydroplastics transforms the static dry network into the hydration state, which is in imbalanced polar environments, enabling the molecular network to exhibit enhancement effect during subsequent dehydration.

Molecular network rearrangement and S-S crosslinking during the process of establishing balance

To further elucidate the mechanism of the zipper model, we conducted more investigations. As shown in Fig. 3a and Supplementary Fig.20, the length and width of CCMA hydroplastics shrank by approximately 6.7% during dehydration. This shrinkage phenomenon is attributed to the elastic capillary forces generated during water evaporation, which produce powerful retracting force that pulls molecular chains into close contact—a process known as physical collapse[39] (Fig. 3b). Simultaneous PCMW images of the carboxyl (-COOH) and hydroxyl (-OH) regions reveal pronounced spectral intensity changes primarily observed during the early drying phase (Fig. 3c and Supplementary Fig.S21, <150 s). This indicates that dynamic hydrogen bond evolution predominantly occurs in the initial stage of drying, with dimer cross-linking between carboxyl groups occurring during molecular chain retraction. Moreover, the creep-strain curve of CCMA hydroplastic stabilizes after 300 seconds during dehydration, demonstrating that the internal S-S network limits uncontrolled shrinkage of CCMA (Fig. 3a). Consequently, the shrinkage observed is only 6.7%. Furthermore, storage modulus (E’) indicates that at 200°C, CCMA hydroplastics maintains a higher modulus compared to CCM film, suggesting that the presence of TA also prevents structural collapse when the hydrogen bond network weakens (Fig. 3d). Additionally, the Tan δ curve (Supplementary Fig.22) reveals that CCMA exhibits broad peaks between 120°C and 200°C, indicating that the S-S network limits molecular motion. Furthermore, compared to conventional PE plastics, CCMA hydroplastics maintain their original dimensions at temperatures as high as 200 ℃, demonstrating their exceptional thermal stability (Supplementary Fig.23).

To investigate the role of TA in the physical collapse process, experiments are conducted. Significant enhancement of the S-S band in Raman spectra at different drying times indicates polarity-induced local enrichment of TA groups during dehydration (Supplementary Fig.24), leading to increased local S-S concentration[26]. The localized enrichment of TA groups is attributed to environmental polarity mismatch caused by dehydration. Therefore, we calculate the binding energy under solvation conditions. Cellulose and carboxyl groups exhibit strong affinity for water and each other (Fig. 2g). In contrast, the hydrophobic TA segments interact weakly with the water environment (Fig. 3e). Therefore, water molecules preferentially detach from TA chains during dehydration, while the cellulose backbone remains stable due to strong hydration. Furthermore, cellulose chains tend to bind to themselves and to carboxyl groups due to their significant polarity differences (Fig. 2a, Cellulose ~5.2 D, TA ~3.6 D). Consequently, the hydrophobic segments of TA extend from dense cellulose chains and form localized aggregation regions[40].

Furthermore, the red shift of the peak indicates that the cross-linked S-S bonds are subjected to tensile stress imposed by collapsed molecular chains. Moreover, a distinct time lag exists between the bonding process and the physical collapse process. PCMW analysis of Raman spectra (Fig. 3f) indicates that the S-S signal intensity undergoes significant changes only during the late dehydration stage (>150 s). This temporal sequence aligns with the local aggregation of the TA hydrophobic segment.

Furthermore, we monitored the hydration state changes of CCMA hydroplastics through DSC at different drying times[23] (Fig. 3g). The endothermic peak of CCMA hydroplastics at 0°C gradually shifts to -8°C before eventually disappearing. This phenomenon indicates that free water (Fw) undergoes spatial confinement and interacts with contracting molecular chains, forming bound water (Bw). The final disappearance indicates that bulk water has been completely removed. Notably, the peak shift from -15°C to -45°C until its disappearance indicates that the bound water is tightly confined within a dense network of S-S bonds, transforming into unfrozen bound water. Furthermore, we performed 2D-COS analysis on the DSC spectra (Supplementary Fig.25). According to Noda's rule, the consumption of free water precedes the stabilization of bound water. This indicates that the evaporation of bulk water forces the remaining water molecules into the binding sites of collapsed molecular chains.

Furthermore, we observe intense asynchronous cross-peaks between the free water peak (DSC) and the -OH/-COOH region (IR) through heterospectral 2D correlation spectroscopy (Fig. 3h). This phenomenon indicates that the consumption of initial free water precedes the group flipping of TA and the reconfiguration of dynamic hydrogen bonds. It confirms that the evaporation of free water generates capillary forces, subsequently pulling and rearranging the molecular chains into a dense network. Here, we correlate the physical collapse (-OH/-COOH changes) with chemical locking (S-S bond formation) (Fig. 3i). According to Noda's rule, the reorganization of the hydrogen bond network precedes S-S bond formation. It further confirms that physical collapse causes TA segments to aggregate, leading to S-S cross-linking. Moreover, the significant increase in S-S peaks is closely associated with the disappearance of the bound water peak (located between -15 and -45 °C) (Supplementary Fig.26). This indicates that the formation of S-S bonds traps frozen water within the network, converting it into non-frozen water.

The structural effects of physically induced S-S crosslinking are clearly reflected in 1D WAXD (Fig. 3j). The primary diffraction peak of dehydrated CCMA hydroplastics shifts toward lower 2θ angles (20.13° to 19.77°). According to Bragg's law, this shift corresponds to an increase in the interlayer spacing (4.41Å to 4.50Å) between molecular chains. This is attributed to the S-S bonds effectively expanding the interlayer space, which remains stable even after 10 cycles.

Therefore, we elucidate the mechanism (Fig. 3k) by which water molecules influence the CCMA molecular network (zipper model). The different polarity between water (2.0 D), cellulose (5.21 D) and TA side chain (3.6 D) induces molecular network rearrangement. Hydrophilic -COOH groups become exposed to the environment when water molecules interact with amphiphilic TA segments. Water penetration disrupts the internal hydrogen bond network, causing network plasticization. Notably, strong capillary forces tighten the molecular chains during free water removal. Furthermore, TA hydrophobic segments undergo local aggregation, triggering S-S re-crosslinking as water continues to be removed.

Fig. 4. Water-induced enhanced mechanical and shape programming. a Tensile strength of CCM and CCMA hydroplastics in L-direction. **b** Mechanical performance of CCM and CCMA hydroplastics under hydration-dehydration cycles in L-direction. **c** Mechanical comparison between CCMA hydroplastics and other hydroplastics[14,18-21,41]. **d** Water-programmed deformation and shape recovery of CCMA hydroplastics. **e** Wet strength. **f** Mechanical properties curve of CCMA-2 after prolonged immersion in water (14 days). **g** Mechanical performance of CCM and CCMA hydroplastics under hydration-dehydration cycles in R-direction. **h** 2D WAXD of CCMA under 0 and 5 hydration-dehydration cycles; azimuthal scanning at Φ (from 0°- 360°) are indicated. **i** Hermann Orientation Factor (*f*) of CCMA under 0 and 5 hydration-dehydration cycles. **j** Crystallinity of CCM and CCMA under dehydration. **k** Changes in the thickness and bulk density of CCMA-2 during dehydration. **l** Mechanism Diagram. The error bars for **b** represent mean ± standard deviation (n = 3 independent samples).

Enhanced mechanical performance and shape programming under the enhancement effect of water.

To investigate the effect of the zipper model on the strength and toughness of CCMA water-based plastics, we conducted extensive mechanical testing. The incorporation of TA enlarges the cellulose network crystalline region[42] (Supplementary Fig.27), crosslink density (Supplementary Table 4), $F_{H\text{-}OH}$ (Supplementary Fig.8) and $F_{H\text{-}CO}$ (Supplementary Fig.16). Thus CCMA hydroplastics exhibit high tensile strength of 177 MPa, which is 52% higher than that of pristine cellulose (Fig. 4a and Supplementary Fig.28). However, excessive TA loading disrupts the ordered arrangement of cellulose chains due to spatial crowding, resulting in reduced molecular irregularity (Supplementary Fig.29 and Supplementary Table 4). It is worth noting that this strength is dynamically changing. Tensile strength (177 MPa) reached

203 MPa after 10 hydration-dehydration cycles (Fig. 4b) and maintained mechanical stability even after 40 cycles (Supplementary Fig.30). Exceptional mechanical strength surpasses that of conventional plastics such as polyethylene terephthalate (PET) and polypropylene (PP) (Fig. 4c, Supplementary Table 1).

CCMA hydroplastics exhibit exceptional water-programmable shape performance through dynamic reversibility (Fig. 4d). Water can plasticize the network for programming (Supplementary Fig.31), while dehydration fixes the special shape within 5 minutes. Additionally, the differing water absorption rates of CCMA hydroplastics at various temperatures (30, 50, 70°C) indicate that water is a crucial factor in maintaining their plasticized state (Supplementary Fig.32). Furthermore, CCMA hydroplastics are programmed into complex shapes during hydration, and these intricate forms remain unchanged after water evaporation (Supplementary Fig.33).

Furthermore, the wet strength of CCM film decreased to 20 MPa due to the disruption of hydrogen bond networks by water, whereas CCMA hydroplastic maintained excellent wet strength of 40–51 MPa accompanied by enhanced elongation (Fig. 4e). Under high humidity conditions (80% and 90% RH), CCMA hydroplastics still maintain excellent tensile strengths (87.4 MPa and 78.8 MPa, respectively) (Supplementary Fig.34). Moreover, CCMA hydroplastics exhibit o Simultaneous PCMW images of r prolonged immersion (14 days). Notably, mechanical strength can still increase to 200 MPa after drying (Fig. 4f, 14 days). These phenomena indicate that the S-S covalent network ensures that CCMA hydroplastic remains insensitive to water (preventing excessive swelling caused by water) while responding to water (facilitating plasticization and programming).

Importantly, the strength of transverse mechanics (Fig. 4g. R-direction) closely matches that of longitudinal strength (Fig. 4b, L-direction). The consistent longitudinal and transverse mechanical performance result from network densification during dehydration, both in the longitaudinal and transverse directions (Fig. 3a).

To elucidate the mechanism behind this enhancement, we conducted further testing. The enhanced diffraction intensity in the 2D WAXD pattern (Fig. 4h and Supplementary Fig.35) suggested that more amorphous regions have transformed into ordered crystalline regions. Changes in the Hermann orientation factor (f) indicate (Fig. 4i) that molecular chains self-assemble into highly oriented regions under the induction of water during repeated hydration-dehydration cycles. This is consistent with the results observed by SEM images (Supplementary Fig.36). This characteristic is further confirmed by changes in crystallinity (Fig. 4j and Supplementary Fig.37). Compared to CCM, the increased crystallinity of CCMA hydroplastics indicates that water guides disordered segments to arrange into ordered crystalline domains during dehydration. In addition, the increase in $F_{H\text{-}OH}$ (Supplementary Fig.38-39) and carbonyl peak area ratio (Fig. 2h) following dehydration also suggests that the molecular chains underwent plasticization, densification, and stabilization. Moreover, In-plane shrinkage and thickness expansion reduce bulk density of CCMA hydroplastic during the hydration-dehydration cycles (Fig. 4k). This phenomenon demonstrates that the rapidly formed S-S network effectively prevents vertical collapse induced by capillary forces. Therefore, these results confirm that the mechanical enhancement mechanism under hydration-dehydration cycles is driven by network densification, which is induced by internal capillary forces, polarity-driven aggregation and S-S recrosslinking.

As shown in Fig. 4l, the network densification and polarity-driven S-S recrosslinking guides molecular chains into a highly oriented ordered state during dehydration. The mechanical self-reinforcement and shape plasticity of CCMA hydroplastics demonstrate the unique advantages of the zipper model.

Water-induced adhesion tuned by polarity and hydrogen bonding

In addition to shape processing and mechanical enhancement, CCMA hydroplastics exhibit strong adhesion during hydration-dehydration cycles (Supplementary Fig.40). The intensity shift of the C=C bond in the TG-IR spectra (Fig. 5a and Supplementary Fig.10) and the change in the ratio of sp^2 C-C to sp^3 C-C bonds (Fig. 5b and Supplementary Fig.6) indicate the successful grafting of TA. Furthermore, the presence of S-S and C-S bonds in the CCMA structure confirms that TA molecules participated in the formation of the multi-network architecture (Fig. 5c). The TA side chain endows CCMA hydroplastics with excellent adhesive properties. Moreover, two pieces of hydroplastics can be rapidly and reversibly bonded together by adding water at the interface (Fig. 5d and Supplementary Movie). The adhesive force is strong enough for the CCMA-3 hydroplastics to lift 1-kilogram weight (Fig. 5e).

Furthermore, the increase in adhesion strength to 37 MPa with rising TA content demonstrates the critical role of COOH and S-S in adhesive performance (Fig. 5f). Furthermore, we prepared a control film named CCMC using 1-hexanethiol (lacking -COOH and S-S bonds) as a contrast. The absence of water-induced adhesion and mechanical self-enhancement in this CCMC film demonstrates that water molecules do not exert a reinforcing effect within it, thereby validating the potential advantages of our strategy (Supplementary Fig.41). Moreover, sufficient water molecules are necessary to achieve strong adhesion strength (Fig. 5g). The minimum water volume fraction required to activate adhesion is approximately 30.4% (25 ℃, 4 mins), corresponding to 70% RH (Supplementary Table 5). Furthermore, CCMA hydroplastics exhibit good solvent resistance (Supplementary Fig.42). Moreover, solvents with varying polarities and pH values further elucidate the respective roles of hydrogen bonding and S-S cross-linking in bonding (Fig. 5h). Under extreme pH conditions (pH 3/13), CCMA hydroplastics maintained adhesion strengths of 16–32 MPa even when internal hydrogen bonds were disrupted. This remarkable strength demonstrates that S-S crosslinking re-establishes adhesion despite hydrogen bond disruption, ensuring adhesive stability. Conversely, negligible adhesion in nonpolar solvents (e.g., petroleum ether) confirms that the absence of carboxylate hydration inhibits subsequent S-S crosslinking. Thus, these phenomena indicate that carboxylate hydration initiates adhesion, while S-S recrosslinking stabilizes adhesion. Crucially, the repeated plasticization of carboxyl groups (Fig. 2h) ensures the presence of renewable bonding sites, enabling CCMA hydroplastics to generate stable adhesion of approximately 37 MPa during repeated hydration-dehydration cycles (Fig. 5i).

Moreover, the enrichment of S elements at the bonding interface indicates the crucial role of S-S crosslinking in adhesion[26](Fig. 5j). This is consistent with the S-S enrichment mechanism mentioned. Furthermore, the increase in thickness of the CCMA hydroplastic demonstrates the enrichment of TA’s hydrophobic segments to resist volume collapse during dehydration (Fig. 4k). Therefore, we propose a mechanism elucidating the adhesion process (Fig. 5k). Water molecules form interfacial hydrogen bonds with carboxyl groups exposed on the surface of CCMA hydroplastics, driven by polarity. Simultaneously, internal diffusion of water molecules promotes molecular chain rearrangement and local enrichment of the TA hydrophobic segment. During dehydration, the recrosslinking of disulfide bonds re-anchors the contacting CCMA hydroplastic networks, generating strong and reversible adhesive forces.

Processability and degradability demonstration of CCMA hydroplastics.

CCMA hydroplastics can be mass-produced by solution casting processes to form uniform, transparent films over large areas (Fig. 6a), confirming their compatibility with scalable production processes. In the area of sealing, with excellent antibacterial properties (Supplementary Fig.43), barrier properties (Supplementary Fig.44), and high transparency (Fig. 1c), CCMA hydroplastics can be used as ecofriendly packaging materials (Supplementary Fig.45). Upon contact with water, the two films can be firmly bonded and sealed (Fig. 6b) without the need for external adhesives or heat, which demonstrates the material's potential as a sustainable, low-energy alternative to petroleum-based plastic packaging. In addition, CCMA hydroplastics do not produce small-sized particles during the bonding process compared to conventional tapes (Supplementary Fig.46), which speaks volumes about the safety of CCMA hydroplastics in packaging. Moreover, CCMA hydroplastics exhibit excellent repair capabilities. As shown in Fig. 6c, only a small amount of water is needed to effectively repair fractured surfaces or damaged substrates at room temperature and without external pressure. Furthermore, CCMA's excellent UV resistance enables it to be used in UV-radiation-resistant materials with very strong potential (Supplementary Fig.47 and Supplementary Table 6). In addition to static applications, CCMA hydroplastics can be useful in dynamic and flexible environments, such as soft robots. Fig. 6d-g illustrates the effect of integrating the material into a soft interface, where water-responsive properties enable temporary actuation. The actuation is due to the water-blocking properties of CCMA, which allow for localized swelling and pressure effects (Supplementary Fig.44). Rapid water evaporation (5 minutes) stabilizes these motions through covalent S-S bonds and hydrogen bond rearrangement (Supplementary Fig.48), thereby achieving a balance between flexibility and rigidity.

Together with its reprogrammable ability and mechanical performance, CCMA hydroplastics have strong potential to serve as a sustainable alternative to traditional petroleum-based plastic. To demonstrate, some hydroshaped CCMA hydroplastics consumer product prototypes are presented in Fig. 6h. Moreover, CCMA hydroplastics can be cast into specific shapes using molds (Fig. 6i). Thicker CCMA hydroplastics are produced to better resemble traditional plastics, with water-programmed hooks capable of bearing weight and spiral anti-choke handles (Fig. 6j and Supplementary Fig.49). Besides, compared to other engineering plastics (such as PP and PE plastics), CCMA hydroplastics have excellent soil biodegradability (Fig. 6k).

Methods

Ethics statement

The wet flexibility test for bioplastics has been approved by the participants.

Materials

Microcrystalline cellulose (MCC, about 10 μm in size) was purchased from Sinopharm Chemical Reagent Co., Ltd. Commercial MCCs. ±-α-Thioctic acid (99%) and stannous octoate (95%), 1-Hexanethiol (94%(GC-MS)) were purchased from Shanghai Titan Technology Co., Ltd, N-N-Dimethylacetamide (Dmac, AR, 99%), Pyridine (AR, ≥99%), Cinnamoyl chloride (97%) were purchased from Shanghai Een Chemical Technology Co., Ltd. LiCl (ACS reagent, ≥99%) was purchased from Aladdin Reagent (Shanghai) Co. Ltd. All chemicals involved in the solvent resistance tests, including Fomic acid (95%), Petroleum ether (AR bp60-90°C), NaOH (97%) were purchased from Aladdin Reagent (Shanghai) Co. Ltd., Ammonia (25-28%), Acetic acid (AR, 99.5%), Methanol (99.5%) were purchased from Shanghai Macklin Biochemical Co., Ltd, Ethylene glycol (99%), Silicone oil was purchased from Dow Corning Co., Ltd. Deionized (DI) water obtained from a laboratory water purifying system was used throughout the experiments. Unless otherwise stated, all of the chemicals were directly used without further purification.

Synthesis of CCMA hydroplastics with different mass ratios

The cellulose solution is prepared by dissolving and stirring MCC in a Dmac/LiCl solvent system. 1.5g MCC is dissolved by stirring at 120 °C with 40ml Dmac and 3g LiCl. 1.3 equivalents of MCC in cinnamoyl chloride and pyridine are added to the cellulose solution respectively, and stirred at a constant speed for 2h at 70°C to form a CCM solution. CCM gel is formed by solution casting method, and then the solvent is replaced in ethanol for 1.5h. CCM plastics are generated after air drying for 8h. Different amounts of α-Thioctic acid (0.5, 1, 1.5 g) were added to CCM solution (20 mL), along with 0.5 wt% stannous octanoate. CCMA solutions containing different masses of α-Thioctic acid were designated as CCMA-1/2/3 solution. CCMA solution was formed by stirring at 70°C for 3 hours. The CCMA sol was prepared via casting and air-dried at room temperature (25°C) for 8 hours, yielding CCMA hydroplastics (CCMA-1/2/3).

Prepare of CCMC plastics as a control

1.5g 1-Hexanethiol are added to the CCM solution (20 mL), stirred at 70°C for 3h, and CCMC solution is formed by catalysis of stannous octoate (0.5%wt). The CCMC sol was prepared via casting and air-dried at room temperature (25°C) for 8 hours, yielding CCMC plastic.

Characterization

The morphology was observed by using field emission scanning electron microscopy (FE-SEM, ULTRA55, Carl Zeiss, Germany) with an accelerating voltage of 3.0 kV. The elemental analysis was investigated by energy dispersive X-ray spectrometer (EDX). Analyze the chemical structure (FTIR) of the materials within the measurement range of 4000-400 cm^{-1}, at a resolution of 2 cm^{-1}. The transparency properties were tested by using a UV–Vis spectrophotometer (UH4150, Hitachi, Japan) at the wavelength range. The water contact angles were measured by a DSA25 Drop Shape Analyzer (KRÜSS, Hamburg) with 5 μL of deionized water. Thermal stability (TGA) was tested by using thermogravimetric analyzer (TG209 F1, Netzlsch) in the temperature range of 30–800 ˚C (nitrogen atmosphere) at a rate of 20 ◦C min^{-1}. The decomposition gases generated during the thermal degradation of TG were transferred to a high temperature infrared gas cell using nitrogen gas through a high temperature gas conductor. Each sample was synthesized from these FTIR spectra of decomposed gases into a TG–FTIR (temperature–wavelength) three–dimensional spectrum. Measurements were performed on a DSC RCS90 system from TA instruments. Each sample was heated from -90 °C to 10 °C at a rate of 5 °C/min. The storage modulus of the samples was determined using Netzsch DMA303. The oscillation frequency was 1.0 Hz. Raman spectrometer (ThinVia) with 785 nm excitation wavelength. The creep test equipment is electronic universal testing machine UTM5300H, manufactured by Shenzhen Sansi Zongheng Co., Ltd. The *XPS* spectrometer was operated in constant analyzer energy (CAE) mode, using a 1 eV step size and an Al Kα X–ray source (1486.6 eV). Split–peak fitting was performed by *XPS* Peak 41 to identify the chemical states and percentages of different valence states. The ^{1}H NMR spectra were performed using Bruker Avance 400 NMR spectrometer and using dimethylsulfoxide (DMSO) as solvent. The zeta potential is tested using the SurPASS solid surface zeta potential tester produced by Anton Paar, Austria. ATR-IR spectra were recorded by using IS50 Fourier Transform Infrared Spectrometer (Thermo Electron, USA). The spectra were subject to ATR correction, smoothing and baseline correction and being normalized. The two-dimensionalcorrelation spectroscopy (2DCOS) was performed using 2Dshige software. In the resulting 2DCOS and PCMW2D graphs, the red and blue colored regions are defined as positive and negative intensities, respectively. A window size of 5 was chosen for the development of the synchronous PCMW2D maps. Finally, the contour maps of PCMW2D were plotted by the Origin 2024.

Mechanical Test

Tensile properties were characterized by using an Instron 5943 universal testing machine. The dimensions used were 1×4 cm strips with a thickness of 0.02 mm (measured using Digital Display Thickness Gauge).

Testing was conducted in a constant temperature and humidity environment at 25°C and 40% RH. Test parameters: loading rate of 1 mm/min. Error bars in the manuscript represent mean ± standard deviation (n = 3 independent samples). Re-measure the dimensions of the shrunken film during the dehydration process and conduct mechanical testing. Adhesive strength testing is conducted after complete adhesion with water (5 minutes), following the steps outlined above.

Water vapor permeation (WVP)

The film was packaged in a 10 mL sample bottle (effective area: 235 mm^2) in an autoclave at 120 ◦C for 10 min at 110 kPa. The WVP through the system was almost completed after the temperature cooled to room temperature, and the condensed water in the bottle was weighed. The WVP was calculated as follows[43]:

$$\mathrm{WVP} = \Delta \mathrm{m}/(\mathrm{t} \times \mathrm{S} \times \mathrm{P}) \times \mathrm{e} \qquad (1)$$

where Δm is the mass change (kg) of the sample at time t (s), S is the test area (m2), e is the thickness of the system (m), and P is the saturation pressure (Pa).

X-Ray Diffraction analysis

The test was performed by using Cu Kα (1.5418 Å) rays (40 kV, 40 mA). The XRD data were collected from 2θ = 5 to 50° at a scan rate of 5°/min. All the specimens were dried at 60 °C in a constant temperature oven before the test. The empirical method for the calculation of the crystalline index proposed by Segal et al. [44]is

$$CrI = \frac{I_{ac} - I_{\mathrm{am}}}{I_{ac}} \times 100 \qquad (2)$$

Where I_{ac} represents the maximum intensity of the peak (020) of the XRD diffraction pattern of the cellulose sample, i.e., at 20◦ for cellulose II. I_{am} represents the lowest intensity between the plane (110) and (020) (Mahmud et al., 2019; Tran et al., 2020).

WAXD (Wide-Angle X-Ray Diffraction)

WAXD (Wide-Angle X-ray Diffraction) measurements were conducted at Xeuss 2.0. The copper target's light tube power is 30W, with a wavelength of 1.54189 Å; The detector used is a Pilatus 3R 300K, with a single pixel size of 172 µm; The distance from the detector to the sample is 83.4 mm; The scattering vector q (horizontal coordinate, units Å⁻¹) is converted to the 2θ coordinate via the formula: $q = \frac{4\pi \sin\theta}{\lambda}$; Fit2D is used to calculate the geometric azimuthal integrals and Hermann orientation factors for 2D WAXD patterns.

The d-spacing were calculated using the Bragg's Eq[45]:

$$n\lambda = 2d\sin\theta \tag{3}$$

where *n* is an integer; λ is the wavelength of incident wave length; *d* is the spacing between the planes in the atomic lattice, θ is the angle between the incident ray and the scattering planes;

Measurement of bulk density

The sample is rectangular in shape, with dimensions of 40 × 10 × 0.02 mm³ (length × width × thickness). Weights were recorded, and the volume was calculated. The process was repeated three times, and the average values were calculated for accuracy.

Molecular dynamic simulation (MDS)

All molecular dynamic simulations were conducted using Materials Studio 2020[46] software in this work, and began with the construction of the molecular models for CCM and CCMA. Subsequently, the Forcite module[47,48] was used to optimize the molecular structure with COMPASSII[49] as the force field to release internal stress in the system. During the geometric optimization process, the convergence threshold for maximum energy change, maximum force convergence threshold, and maximum displacement convergence threshold are 0.001 kcal mol^{-1}, 0.5 kcal mol^{-1} Å^{-1}, and 0.015 Å, respectively. Then, 140 ps dynamic simulation was performed under the constant-pressure, constant-temperature ensemble (NPT) at 0.0001 GPa and 298 K to check the course of density fluctuations until the density-time curve was stable. In the progress of MDS, electrostatic is calculated using Ewald, while van der Waals is calculated using atom base. The precise Nose-Hoover[50] temperature control mode and Berendsen pressure control mode are used in the dynamic process. Afterward, the final simulated structure will undergo MSD (Mean Square Displacement) analyses and the radial distribution function (RDF).

The binding energy was calculated using the DMol3 module[51-53] of the Materials Studio software package, and two generalized functions, Perdew-Burke-Ernzerhof (PBE)[54-56] was chosen for this study. All calculations were performed in the framework of a plane-wave basis set, and the dual-numerical plus polarization (DNP) basis set[51] was used considering the balance between computational efficiency and accuracy. During the geometry optimization, the force convergence criterion is set to 0.01 eV Å^{-1} and the energy convergence criterion is 1×10^{-5} Ha to ensure the stability of the structure and the accuracy of the energy calculation. The binding energy was calculated by the following formula.

$$E_{binding} = E_{complex} - \left(E_{partA} + E_{partB}\right) \quad (4)$$

where $E_{complex}$ is the total energy for the two structures in the system

The initial structures of Cellulose, H_2O, TA were drawn with the help of Materials Studio in the electrostatic potential calculation(ESP) and molecular frontier orbitals. The B3LYP method and the 6-

311G (d, p) basis set of Dmol3 module were used to calculate each molecule. All geometry optimizations and energy calculations were performed using the DMol³ module. To mimic the wet environment, a continuous solvation model (COSMO) using water as the solvent was applied. Note on Limitations: It should be acknowledged that these DFT calculations simulate simplified molecular models. While they provide robust qualitative trends regarding relative binding affinities, they may not quantitatively capture full complexity of the bulk condensed phase.

In Dipole moment, the initial TA structure was drawn with the help of the Materials Studio software package. The B3LYP [57] method and the 6-311G (d, p)[58] basis set were used for calculations on each molecule. The Multiwfn package was used to analyze IGM isosurfaces and RDG scatter plots. The VMD software was used for visualizing the analyzed data[31,59].

Optical Test

According to AATCC 183:2000 standard, the ultraviolet protection factor (UPF) and percentages of UVA and UVB radiation blocking were calculated with UV-2000F Textiles UV Factor Tester (Labsphere Company, USA) using the following equations[60]:

$$\text{UV protection factor (UPF)} = \frac{\int_{280}^{400} E(\lambda)S(\lambda)\mathrm{d}\lambda}{\int_{280}^{400} E(\lambda)S(\lambda)T(\lambda)\mathrm{d}\lambda} \quad (5)$$

$$\text{UVA blocking (\%)} = 100 - \frac{\int_{320}^{400} T(\lambda)\mathrm{d}\lambda}{\int_{320}^{400} \mathrm{d}\lambda}(\%) \quad (5)$$

$$\text{UVB blocking (\%)} = 100 - \frac{\int_{280}^{320} T(\lambda)\mathrm{d}\lambda}{\int_{280}^{320} \mathrm{d}\lambda}(\%) \quad (6)$$

where E (λ) is the relative erythema spectral effectiveness, S (λ) is the spectral irradiance ($\mathrm{Wm}^{-2}\ \mathrm{nm}^{-1}$), dλ is bandwidth, and λ is wavelength.

Water swelling test

Samples (2 cm × 2 cm) were cut out and then put into the oven at 80 °C for 8 h. After drying, the starting mass of each film sample was weighed out with an analytic balance. After recording, each sample was put into deionized water for 48 h. Then, the mass of the film sample was measured by an analytical balance and recorded. Water absorption can be expressed as:

$$Water absorption = \frac{W_a - W_b}{W_b} \times 100\% \qquad (7)$$

Where is recorded weight after water absorption, W_a W_b is the weight before water absorption.

Chemical cross-linking density

Chemical cross-linking density (V_e) of different samples can be expressed according to the reported equation[61]:

$$V_e = V_{ro}/V_{rf} \qquad (8)$$

$$V_{ro} = \frac{d/\rho_p}{(d/\rho_p) + (A_s/\rho_p)} \qquad (9)$$

$$V_{rf} = \frac{(d - fw)/\rho_p}{(d/fw)/\rho_p + (A_s/\rho_p)} \qquad (10)$$

Where d is the swollen weight of the sample, ρ_p is the density of the bioplastic, f is the volume fraction of TA in the cellulose films and w is the weight fraction of TA and A_s is the amount of deionized water absorbed by the sample. V_{ro} is constant for a particular system. V_{rf} is the volume fraction of chemical crosslinking phase in cellulose films and is calculated using Eq. (8-10).

Calculation of Hydrogen Bonding Coefficients

The hydrogen bonding coefficient (F_{H-CO}) was calculated by curve-fitting of carbonyl band using the

Gauss-Lorentz function[62].

$$F_{H-CO} = \frac{A_H/r_{H/f}}{A_H/r_{H/f} + A_f} \tag{11}$$

where A_f and A_H are the areas of the free peak and the hydrogen bonded component, $r_{H/f}$ is the characteristic adsorption ratio of the above two bands, which is in the range of 1.2–1.75.

The value of F_{H-OH} is calculated according to eq 12.

$$\mathrm{F}_{H-OH} = (A_{\mathrm{H}}/r_{\mathrm{H/a}})/(A_{\mathrm{H}}/r_{\mathrm{H/a}} + A_{\mathrm{a}}) \tag{12}$$

where $\mathrm{A_a}$ and $\mathrm{A_H}$ are peak areas of the free and hydrogenbonded components, respectively, and $\mathrm{r_{H/a}}$ is the intensity ratio of the two peaks

Data availability

All data that support the findings of this study are available within the paper and its supplementary information files or are available from the corresponding authors upon request. Source data are provided with this paper.

References

1 Li, T. *et al.* Developing fibrillated cellulose as a sustainable technological material. *Nature* **590**, 47-56 (2021).

2 Li, T. *et al.* Cellulose ionic conductors with high differential thermal voltage for low-grade heat harvesting. *Nature materials* **18**, 608-613 (2019).

3 Huang, C. *et al.* Recent Advances in Green and Efficient Cellulose Utilization Through Structure Deconstruction and Regeneration. *Advanced Functional Materials*, 2424591 (2025).

4 Kwak, H. *et al.* Biodegradable, water-resistant, anti-fizzing, polyester nanocellulose composite paper

straws. *Advanced Science* **10**, 2205554 (2023).

5 Klemm, D., Heublein, B., Fink, H. P. & Bohn, A. Cellulose: fascinating biopolymer and sustainable raw material. *Angewandte chemie international edition* **44**, 3358-3393 (2005).

6 Mohanty, A. K. *et al.* Sustainable polymers. *Nature Reviews Methods Primers* **2**, 46 (2022).

7 Zhu, Y., Romain, C. & Williams, C. K. Sustainable polymers from renewable resources. *Nature* **540**, 354-362 (2016).

8 Droguet, B. E. *et al.* Large-scale fabrication of structurally coloured cellulose nanocrystal films and effect pigments. *Nature materials* **21**, 352-358 (2022).

9 Heise, K. *et al.* Nanocellulose: recent fundamental advances and emerging biological and biomimicking applications. *Advanced Materials* **33**, 2004349 (2021).

10 Hartmann, F., Baumgartner, M. & Kaltenbrunner, M. Becoming sustainable, the new frontier in soft robotics. *Advanced Materials* **33**, 2004413 (2021).

11 Kang, Y. *et al.* Functionalized 2D membranes for separations at the 1-nm scale. *Chemical Society Reviews* (2024) **53**, 7939–7959 (2024).

12 Isogai, A. Emerging nanocellulose technologies: recent developments. *Advanced Materials* **33**, 2000630 (2021).

13 Zheng, N., Xu, Y., Zhao, Q. & Xie, T. Dynamic covalent polymer networks: a molecular platform for designing functions beyond chemical recycling and self-healing. *Chemical Reviews* **121**, 1716-1745 (2021).

14 Wang, J., Emmerich, L., Wu, J., Vana, P. & Zhang, K. Hydroplastic polymers as eco-friendly

hydrosetting plastics. *Nature Sustainability* **4**, 877-883 (2021).

15 Shao, Y. *et al.* A Tough Monolithic-Integrated Triboelectric Bioplastic Enabled by Dynamic Covalent Chemistry. *Advanced Materials* **36**, 2311993 (2024).

16 Wang, Z. *et al.* Thermally Robust Aramid Triboelectric Materials Enabled by Heat-Induced Cross-Linking. *Advanced Functional Materials* **35**, 2413719 (2025).

17 Wang, J. *et al.* Janus Asymmetric Cellulosic Triboelectric Materials Enabled by Gradient Nano-Doping Strategy. *Advanced Functional Materials*, 2424185 (2025).

18 Gong, K., Hou, L. & Wu, P. Hydrogen-bonding affords sustainable plastics with ultrahigh robustness and water-assisted arbitrarily shape engineering. *Advanced Materials* **34**, 2201065 (2022).

19 Chen, W., Huang, C., Biehl, P. & Zhang, K. Water training initiates spatially regulated microstructures with competitive mechanics in hydroadaptive polymers. *Nature Communications* **15**, 6093 (2024).

20 Zeng, Z. *et al.* Tuning water-cellulose interactions via copper-coordinated mercerization for hydro-actuated, shape-memory cellulosic hydroplastics. *Matter* **7**, 3036-3052 (2024).

21 Koh, J. J. *et al.* Reprogrammable, Sustainable, and 3D-Printable Cellulose Hydroplastic. *Advanced Science* **11**, 2402390 (2024).

22 Wang, S. *et al.* Humidity-adaptive, mechanically robust, and recyclable bioplastic films amplified by nanoconfined assembly. *Aggregate* **5**, e643 (2024).

23 Jing, S. *et al.* The critical roles of water in the processing, structure, and properties of nanocellulose. *ACS nano* **17**, 22196-22226 (2023).

24 Zhou, J. *et al.* Supramolecular Scale Hydrophilicity Regulation Enabling Efficient Dewatering and Assembly of Nanocellulose into Dense and Strong Bulk Materials as Sustainable Plastic Substitutes. *Advanced Materials*, 2415313 (2025).

25 Van Oss, C. J., Chaudhury, M. K. & Good, R. J. Interfacial Lifshitz-van der Waals and polar interactions in macroscopic systems. *Chemical reviews* **88**, 927-941 (1988).

26 Zhang, Q. *et al.* Exploring a naturally tailored small molecule for stretchable, self-healing, and adhesive supramolecular polymers. *Science advances* **4**, eaat8192 (2018).

27 Chung, W. J. *et al.* The use of elemental sulfur as an alternative feedstock for polymeric materials. *Nature chemistry* **5**, 518-524 (2013).

28 Yin, C. *et al.* Aqu-Thermoplastics: Recycling Plastics with Water. *Advanced Functional Materials* **35**, 2417119 (2025).

29 Reed, A. E., Curtiss, L. A. & Weinhold, F. Intermolecular interactions from a natural bond orbital, donor-acceptor viewpoint. *Chemical Reviews* **88**, 899-926 (1988).

30 Lu, T. A comprehensive electron wavefunction analysis toolbox for chemists, Multiwfn. *The Journal of Chemical Physics* **161** (2024).

31 Lu, T. & Chen, F. Multiwfn: A multifunctional wavefunction analyzer. *Journal of computational chemistry* **33**, 580-592 (2012).

32 Ohmine, I. & Saito, S. Water dynamics: Fluctuation, relaxation, and chemical reactions in hydrogen bond network rearrangement. *Accounts of chemical research* **32**, 741-749 (1999).

33 Hou, L., Ma, K., An, Z. & Wu, P. Exploring the volume phase transition behavior of POEGA-and

PNIPAM-based core–shell nanogels from infrared-spectral insights. *Macromolecules* **47**, 1144-1154 (2014).

34 Zhang, W., Wu, B., Sun, S. & Wu, P. Skin-like mechanoresponsive self-healing ionic elastomer from supramolecular zwitterionic network. *Nature Communications* **12**, 4082 (2021).

35 Noda, I. Two-dimensional infrared spectroscopy. *Journal of the American Chemical Society* **111**, 8116-8118 (1989).

36 Lei, Z. & Wu, P. Zwitterionic skins with a wide scope of customizable functionalities. *ACS nano* **12**, 12860-12868 (2018).

37 Czarnecki, M. A., Morisawa, Y., Futami, Y. & Ozaki, Y. Advances in molecular structure and interaction studies using near-infrared spectroscopy. *Chemical reviews* **115**, 9707-9744 (2015).

38 Noda, I. Generalized two-dimensional correlation method applicable to infrared, Raman, and other types of spectroscopy. *Applied spectroscopy* **47**, 1329-1336 (1993).

39 Salem, K. S., Barrios, N., Jameel, H., Pal, L. & Lucia, L. Computational and experimental insights into the molecular architecture of water-cellulose networks. *Matter* **6**, 1366-1381 (2023).

40 Sheng, Y. *et al.* Engineering Water-Stiffening Polymers via PEG-Sidechain-Mediated Microphase Separation. *Advanced Functional Materials* **34**, 2401999 (2024).

41 Ashby, M. F. Materials selection in mechanical design. *Metallurgia Italiana* **86**, 475-475 (1994).

42 Manan, S. *et al.* Bacterial cellulose: Molecular regulation of biosynthesis, supramolecular assembly, and tailored structural and functional properties. *Progress in Materials Science* **129**, 100972 (2022).

43 Li, F. *et al.* Bifunctional reinforcement of green biopolymer packaging nanocomposites with natural

cellulose nanocrystal–rosin hybrids. *ACS Applied Bio Materials* **3**, 1944-1954 (2020).

44 Chundawat, S. P. S. *et al.* Restructuring the Crystalline Cellulose Hydrogen Bond Network Enhances Its Depolymerization Rate. *Journal of the American Chemical Society* **133**, 11163-11174 (2011).

45 Ju, X., Bowden, M., Brown, E. E. & Zhang, X. An improved X-ray diffraction method for cellulose crystallinity measurement. *Carbohydrate Polymers* **123**, 476-481 (2015).

46 Deyab, M., Guo, L. & Mohsen, Q. The efficacy of ammonium ionic liquid to inhibit the parasitic process for Al-air battery. *Journal of Energy Storage* **89**, 111707 (2024).

47 Lin, D., Jiang, M., Qi, S. & Wu, D. Macromolecular structural evolution of polyimide chains during large-ratio uniaxial fiber orientation process revealed by molecular dynamics simulation. *Chemical Physics Letters* **756**, 137847 (2020).

48 Nie, W., Ruan, M., Guo, D. & Liu, X. Design of flexible hydrophobic photocatalytic sheets on polydimethylsiloxane substrates based on carrier migration of Si-O-Ti hybrid bonds for photodegradation of dye molecules. *Applied Surface Science* **616**, 156415 (2023).

49 Möttönen, N. B. & Karttunen, A. J. Mechanical properties of polypropylene–cellulose biocomposites: molecular dynamics simulations combined with constant strain method. *Molecules* **28**, 1115 (2023).

50 Lima, K. A. L. & Ribeiro Júnior, L. A. Formation and stability of nanoscrolls composed of graphene and hexagonal boron nitride nanoribbons: insights from molecular dynamics simulations. *Journal of Molecular Modeling* **29**, 339 (2023).

51 Delley, B. An all-electron numerical method for solving the local density functional for polyatomic molecules. *The Journal of chemical physics* **92**, 508-517 (1990).

52 Delley, B. Fast calculation of electrostatics in crystals and large molecules. *The Journal of physical chemistry* **100**, 6107-6110 (1996).

53 Delley, B. A scattering theoretic approach to scalar relativistic corrections on bonding. *International journal of quantum chemistry* **69**, 423-433 (1998).

54 Perdew, J. P., Burke, K. & Ernzerhof, M. Generalized gradient approximation made simple. *Physical review letters* **77**, 3865 (1996).

55 Perdew, J. P., Burke, K. & Ernzerhof, M. Perdew, burke, and ernzerhof reply. *Physical Review Letters* **80**, 891 (1998).

56 Perdew, J. P., Burke, K. & Wang, Y. Generalized gradient approximation for the exchange-correlation hole of a many-electron system. *Physical review B* **54**, 16533 (1996).

57 Radovic, L. R. The mechanism of CO2 chemisorption on zigzag carbon active sites: a computational chemistry study. *Carbon* **43**, 907-915 (2005).

58 Becke, A. D. Density-functional thermochemistry. III. The role of exact exchange. *The Journal of chemical physics* **98**, 5648-5652 (1993).

59 Humphrey, W., Dalke, A. & Schulten, K. VMD: visual molecular dynamics. *Journal of molecular graphics* **14**, 33-38 (1996).

60 Abdalkarim, S. Y. H. *et al.* Sheet-like cellulose nanocrystal-ZnO nanohybrids as multifunctional reinforcing agents in biopolyester composite nanofibers with ultrahigh UV-shielding and antibacterial performances. *ACS Applied Bio Materials* **1**, 714-727 (2018).

61 Chen, Y. *et al.* Tailoring Hydronium ion Driven Dissociation-Chemical Cross-Linking for Superfast

One-Pot Cellulose Dissolution and Derivatization to Build Robust Cellulose Films. *Acs Nano* **18**, 8754-8767, doi:10.1021/acsnano.3c11335 (2024).

62 Li, F. *et al.* Natural biodegradable poly (3-hydroxybutyrate-co-3-hydroxyvalerate) nanocomposites with multifunctional cellulose nanocrystals/graphene oxide hybrids for high-performance food packaging. *Journal of agricultural and food chemistry* **67**, 10954-10967 (2019).

Acknowledgements

This work was supported by National Natural Science Key Foundation of China (52273095, H. –Y. Y.), Outstanding Youth Project of Zhejiang Provincial Natural Science Foundation (LR22E030002, H. –Y. Y.), and the Key Research and Development Program of Zhejiang Province (Grant No. 2022C01049, H. –Y. Y.)

Author Contributions

G. C. and H. –Y. Y. conceived and designed the idea. G. C., C. H. and H. –Y. Y. designed the experiments, collected and analyzed the data. G. C. papered the experiments and characterizations, analyzed DFT and MD calculations, discussed the results and prepared the manuscript, wrote the manuscript. G. C., C. H., Y. D., Y. Z., Y. C. and K. C. T. designed the experiment.

Competing interests

The authors declare no competing interests.

Fig. 1. Design strategies for the plasticizing and enhancement effects of polarity-driven in CCMA hydroplastics. a–b Synthetic scheme and processing steps of CCMA hydroplastics. **c** The transparency

of CCMA hydroplastics. **d** SEM cross-section of CCMA-2. **e–f** Construction of molecular networks of CCMA hydroplastics. **g** Schematic diagram of dipole-dipole interaction. **h** Schematic illustration of the polarity gradient-regulated molecular chain self-assembly mechanism inspired by zippers. **i** The enhancement effect of water molecules on the overall performance of CCMA hydroplastics. **j** Overall performance of this work compared to other hydroplastics.

Fig. 2. Polarity gradient driven plasticizing and dynamic hydrogen bond evolution in CCMA hydroplastics during imbalanced polarity environment. **a** Dipole distance of TA, CCM, Cellulose, H_2O, CH_3OH and CH_3COOH. **b** Surface zeta potential of CCM and CCMA-2. **c** Dynamic water contact angle of CCM and CCMA-3. **d** Radial distribution function (RDF) of CCMA/H_2O system. **e** IGMH visualization of hydrogen bond between –COOH in TA and H_2O. **f** Binding energies. **g** HOMO-LUMO energy level. **h** Integral area ratios of the band related to different states of C=O. **i** 2D-COS infrared spectra (*v* (OH), *v* (COOH)) under transient infrared spectra during the drying process, the warm colors (red) represent positive intensities, while cold colors (blue) represent negative ones. **j** Hydrogen bond competition and dynamic evolution under hydration-dehydration cycle. The error bars for **b** represent mean ± standard deviation (n = 3 independent samples).

Fig. 3. Molecular network rearrangement and network densification during imbalanced polarity environment. **a** Shrinkage change of CCMA hydroplastics under hydration-dehydration cycles; Creep testing of CCMA-2 in wet and dry conditions. **b** Schematic diagram of physical collapse caused by

capillary forces. **c** Perturbation-Correlated Moving Window (PCMW) 2D Correlation Spectra calculated from IR spectra (*v* (OH)) of CCMA-3 hydroplastics during dehydration process. **d** Storage modulus curve. **e** Binding energy. **f** PCMW 2D Correlation Spectra calculated from Raman spectra (*v* (S-S)) of CCMA-3 hydroplastics during dehydration process. **g** DSC curves at different dehydration times. **h** Synchronous and asynchronous spectra of CCMA hydroplastics heterogeneous 2D spectra (*v* (OH), *v* (COOH)) and DSC spectra (*v* (Bw), *v* (Fw)). **i** Synchronous and asynchronous spectra of CCMA hydroplastics heterogeneous 2D spectra (Raman (v (S-S)) and DSC spectra (*v* (Bw), *v* (Fw)). **j** 1D WAXD of CCMA under 0 and 5 hydration-dehydration cycles; d- space (d): cycle 0 =4.41 Å; cycle 5 = 4.50 Å. **k** Mechanism diagram. The warm colors (red) in **c f h i** represent positive intensities, while cold colors (blue) in **c f h i** represent negative ones.

Fig. 4. Water-induced enhanced mechanical and shape programming. a Tensile strength of CCM and CCMA hydroplastics in L-direction. **b** Mechanical performance of CCM and CCMA hydroplastics under hydration-dehydration cycles in L-direction. **c** Mechanical comparison between CCMA hydroplastics and other hydroplastics[14,18-21,41]. **d** Water-programmed deformation and shape recovery of CCMA hydroplastics. **e** Wet strength. **f** Mechanical properties curve of CCMA-2 after prolonged immersion in water (14 days). **g** Mechanical performance of CCM and CCMA hydroplastics under hydration-dehydration cycles in R-direction. **h** 2D WAXD of CCMA under 0 and 5 hydration-dehydration cycles; azimuthal scanning at Φ (from 0°- 360°) are indicated. **i** Hermann Orientation Factor (*f*) of CCMA under 0 and 5 hydration-dehydration cycles. **j** Crystallinity of CCM and CCMA under dehydration. **k**

Changes in the thickness and bulk density of CCMA-2 during dehydration. **l** Mechanism Diagram. The error bars for **b** represent mean ± standard deviation (n = 3 independent samples).

Fig. 5. Water-induced reversible adhesion performance. a TG-IR spectra of CCMA-2. **b** *XPS* spectra of C1*s* regions for CCMA-2. **c** *XPS* signal of S2*p* regions for CCMA-2. **d** Demonstration of water-induced adhesion between two CCMA hydroplastics pieces. **e** Weight-lifting demonstration of CCMA hydroplastics after bonding. **f** Adhesion strength of CCMA hydroplastics at varying TA contents. **g** Relative humidity dependence of adhesion strength of CCMA-3. **h** Effect of solvent polarity on adhesion strength of CCMA-3. **i** Stability of water-induced adhesion performance. **j** Image of two pieces of CCMA hydroplastics adhered together and S-element distribution. **k** Schematic illustration of adhesion mechanism. The error bars for **g, h** represent mean ± standard deviation (n = 3 independent samples).

Fig. 6. Processability and degradability demonstration of CCMA hydroplastics. a Large-area fabrication of CCMA hydroplastics. **b** Water-induced adhesion and packaging application of CCMA hydroplastics. **c** interface-repair demonstration on engineering plastics(PE) by water. **d-g** Simulation of soft robotics under water vapor. **h** Image showing prototypes of hydroshaped commercial products, including stationery holder and bag, made from thickened CCMA hydroplastics. **i** CCMA hydropastic prepared in Type I letter molds. **j** Thicker CCMA hydropastic (1mm) molds into hooks and spiral anti-choke handles through water. **k** Photographs of the soil degradation of CCMA and PE/PP plastic.

Editorial Summary

Assembling cellulose into hydroplastics through water-enhanced effects remains challenging. Here the authors demonstrate that modulating the polarity by using thioctic acid leads to a reconfigured network with enhanced mechanical properties and reversible adhesion.

Peer review information: *Nature Communications* thanks Tian Li, who co-reviewed with Xiwei Shan; Chaoji Chen and the other, anonymous, reviewer for their contribution to the peer review of this work. A peer review file is available

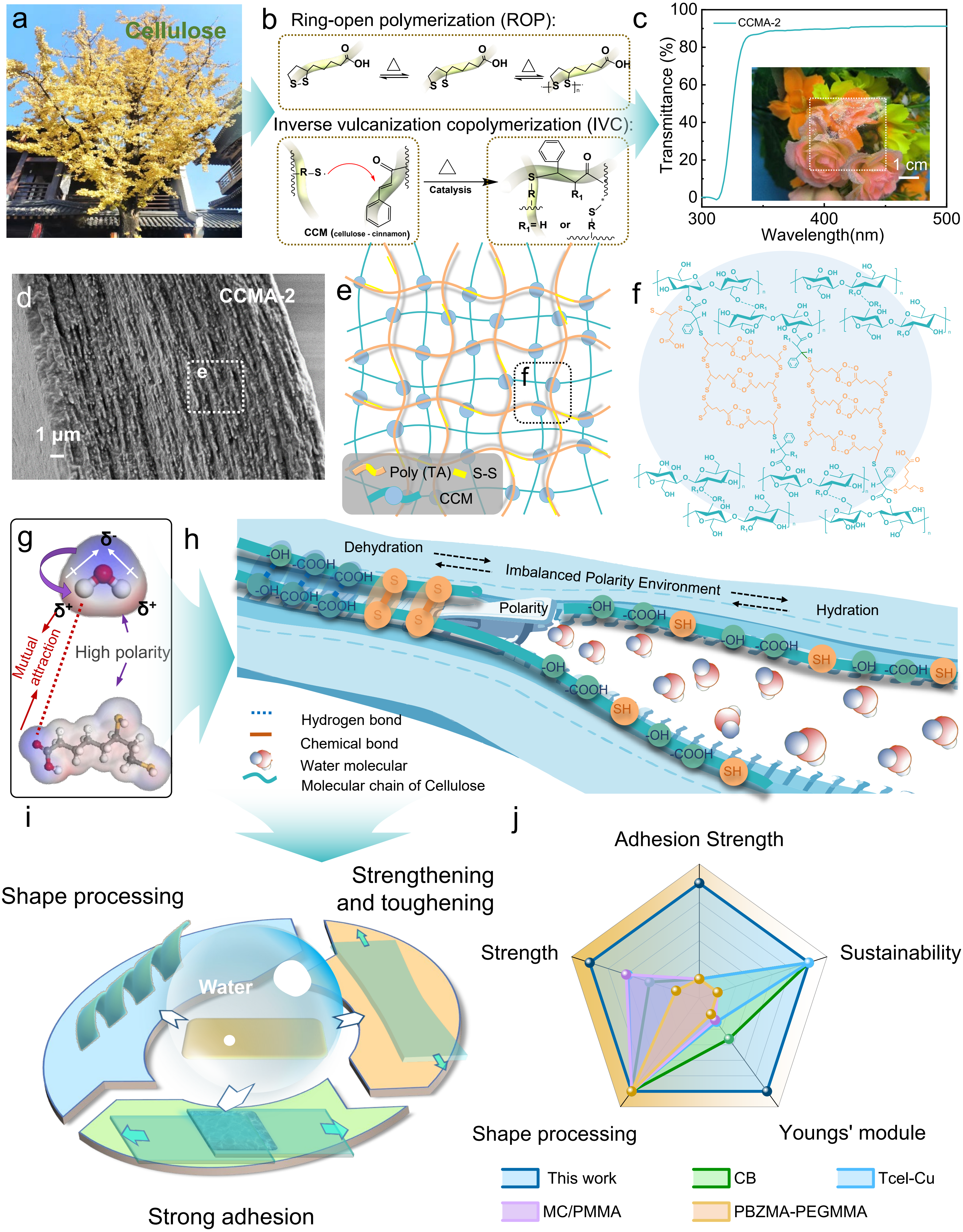
a
Cellulose
b
Ring-open polymerization (ROP):
O
OH
S-S
Inverse vulcanization copolymerization (IVC):
R-S
Catalysis
CCM (cellulose - cinnamon)
S
R
R1
R1 = H or R
c
CCMA-2
Transmittance (%)
Wavelength(nm)
0
20
40
60
80
100
300
400
500
1 cm
d
CCMA-2
e
1 μm
e
f
Poly (TA)
S-S
CCM
f
g
δ-
δ+
δ+
Mutual attraction
High polarity
h
Dehydration
Imbalanced Polarity Environment
Polarity
Hydration
-OH
-COOH
SH
S
Hydrogen bond
Chemical bond
Water molecular
Molecular chain of Cellulose
i
Shape processing
Strengthening and toughening
Water
Strong adhesion
j
Adhesion Strength
Strength
Sustainability
Shape processing
Youngs' module
This work
CB
Tcel-Cu
MC/PMMA
PBZMA-PEGMMA

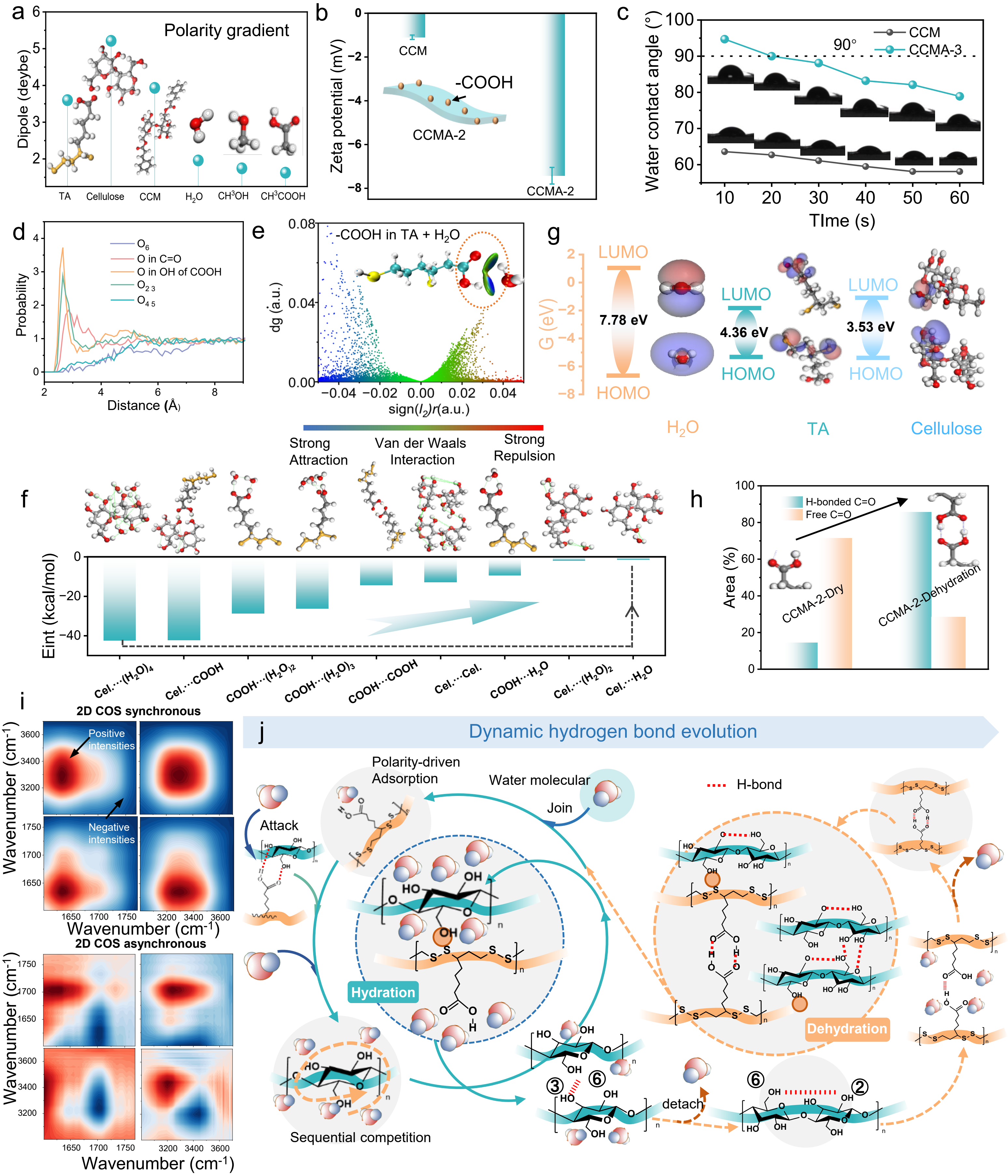
a
Polarity gradient
Dipole (deybe)
TA
Cellulose
CCM
H_2O
CH^3OH
CH^3COOH
b
Zeta potential (mV)
CCM
-COOH
CCMA-2
CCMA-2
c
Water contact angle (°)
90°
CCM
CCMA-3
TIme (s)
d
Probability
O_6
O in C=O
O in OH of COOH
$O_{2\,3}$
$O_{4\,5}$
Distance (Å)
e
-COOH in TA + H_2O
dg (a.u.)
sign(l_2)r(a.u.)
Strong Attraction
Van der Waals Interaction
Strong Repulsion
g
G (eV)
LUMO
7.78 eV
HOMO
LUMO
4.36 eV
HOMO
LUMO
3.53 eV
HOMO
H_2O
TA
Cellulose
f
Eint (kcal/mol)
Cel.···$(H_2O)_4$
Cel.···COOH
COOH···$(H_2O)_2$
COOH···$(H_2O)_3$
COOH···COOH
Cel.···Cel.
COOH···H_2O
Cel.···$(H_2O)_2$
Cel.···H_2O
h
Area (%)
H-bonded C=O
Free C=O
CCMA-2-Dry
CCMA-2-Dehydration
i
2D COS synchronous
Positive intensities
Negative intensities
Wavenumber (cm^{-1})
Wavenumber (cm^{-1})
2D COS asynchronous
Wavenumber (cm^{-1})
Wavenumber (cm^{-1})
j
Dynamic hydrogen bond evolution
Polarity-driven Adsorption
Water molecular
Join
Attack
H-bond
Hydration
Sequential competition
detach
Dehydration
③
⑥
⑥
②

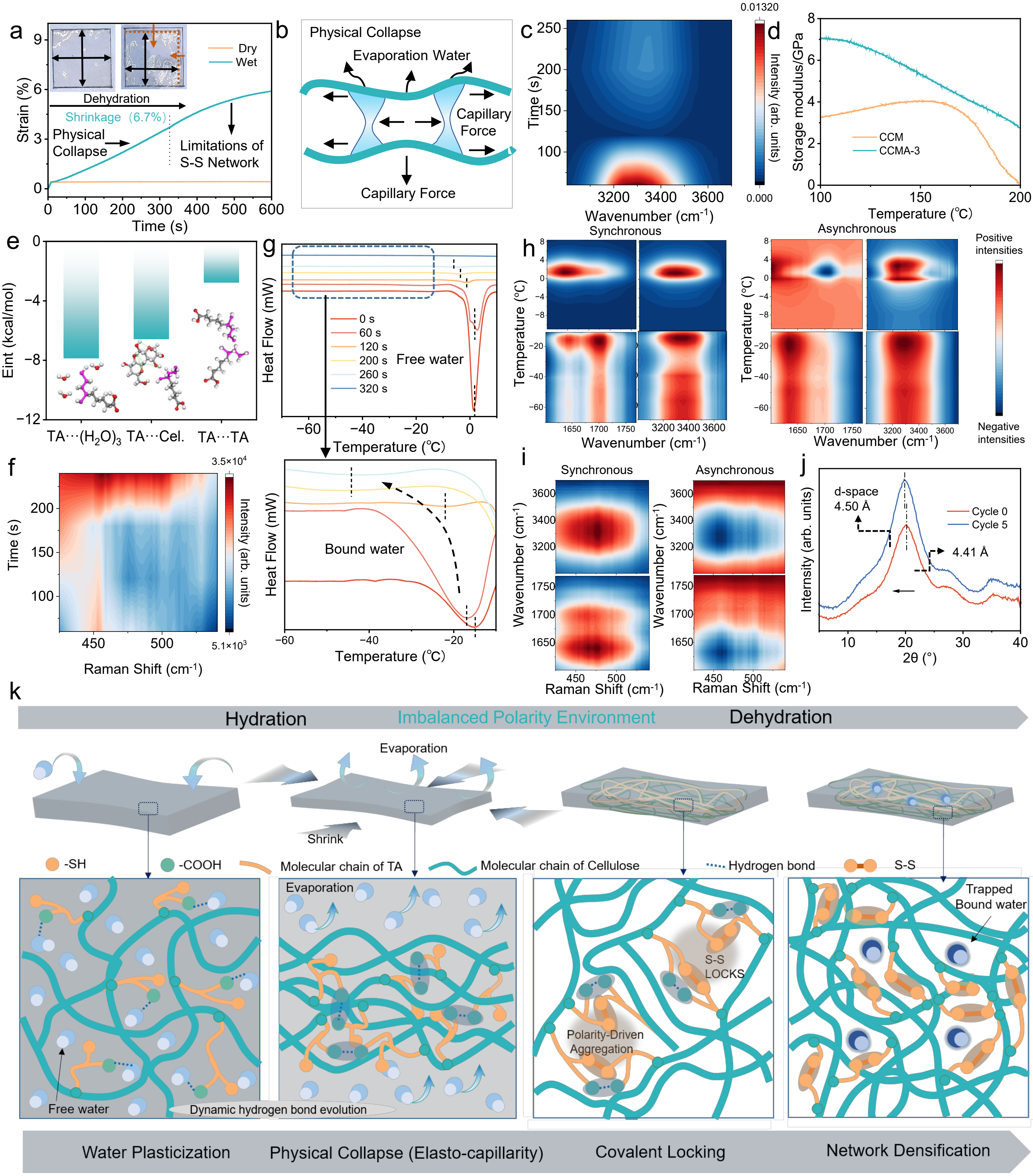
a
Dry
Wet
Strain (%)
Dehydration
Shrinkage（6.7%）
Physical Collapse
Limitations of S-S Network
Time (s)
b
Physical Collapse
Evaporation Water
Capillary Force
Capillary Force
c
Time (s)
Wavenumber (cm-1)
0.01320
0.000
Intensity (arb. units)
d
Storage modulus/GPa
CCM
CCMA-3
Temperature (℃)
e
Eint (kcal/mol)
TA···(H2O)3
TA···Cel.
TA···TA
f
Time (s)
Raman Shift (cm-1)
3.5×10^4
5.1×10^3
Intensity (arb. units)
g
Heat Flow (mW)
0 s
60 s
120 s
200 s
260 s
320 s
Free water
Temperature (℃)
Heat Flow (mW)
Bound water
Temperature (℃)
h
Synchronous
Asynchronous
Temperature (℃)
Wavenumber (cm-1)
Positive intensities
Negative intensities
i
Synchronous
Asynchronous
Wavenumber (cm-1)
Raman Shift (cm-1)
j
Intensity (arb. units)
d-space 4.50 Å
4.41 Å
Cycle 0
Cycle 5
2θ (°)
k
Hydration
Imbalanced Polarity Environment
Dehydration
Evaporation
Shrink
-SH
-COOH
Molecular chain of TA
Molecular chain of Cellulose
Hydrogen bond
S-S
Evaporation
S-S LOCKS
Polarity-Driven Aggregation
Trapped Bound water
Free water
Dynamic hydrogen bond evolution
Water Plasticization
Physical Collapse (Elasto-capillarity)
Covalent Locking
Network Densification

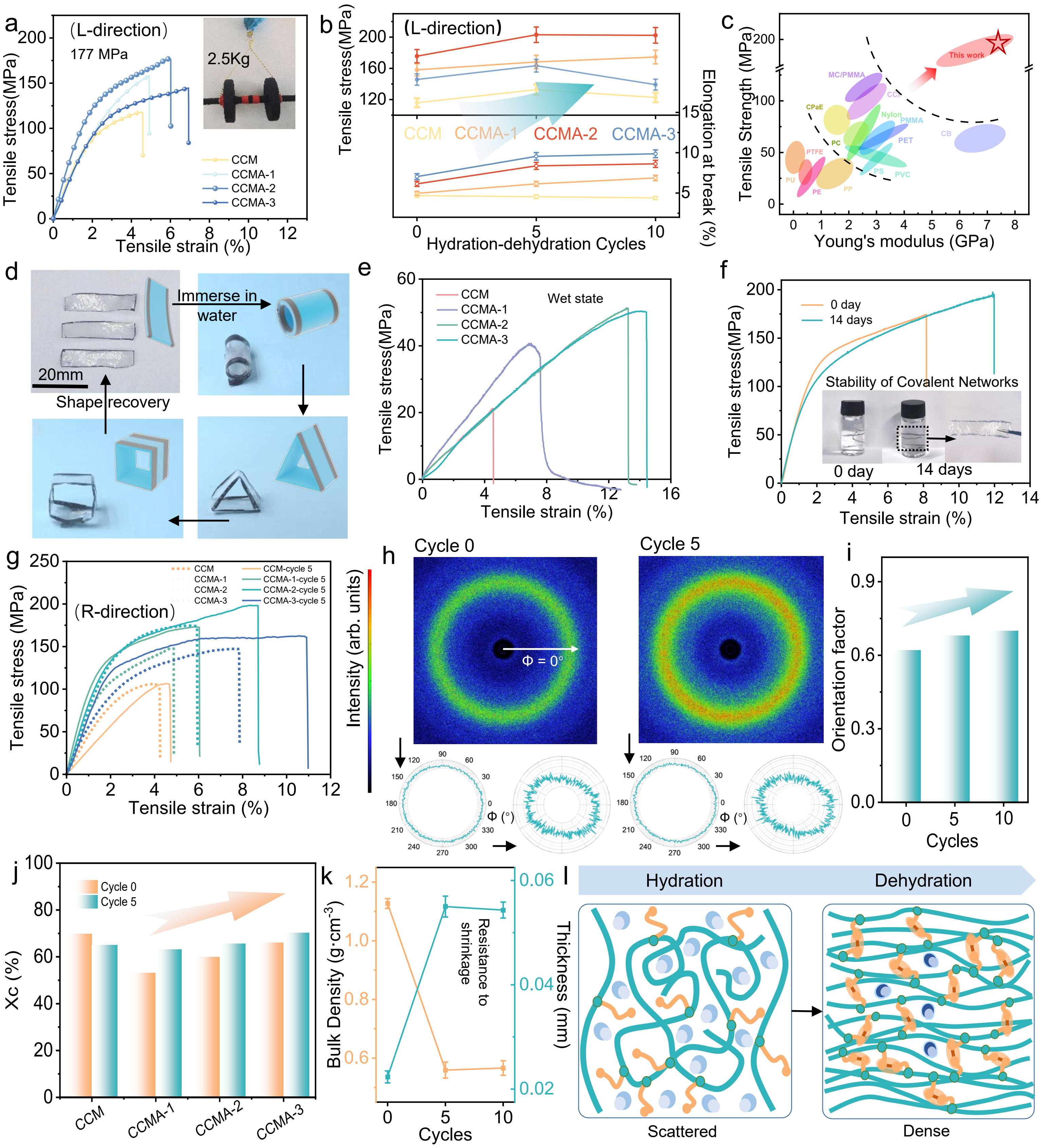
a
(L-direction)
177 MPa
2.5Kg
Tensile stress(MPa)
Tensile strain (%)
CCM
CCMA-1
CCMA-2
CCMA-3
b
(L-direction)
Tensile stress(MPa)
CCM CCMA-1 CCMA-2 CCMA-3
Elongation at break (%)
Hydration-dehydration Cycles
c
This work
MC/PMMA
CCI
CPaE
Nylon
PMMA
PET
CB
PC
PTFE
PU
PE
PP
PS
PVC
Tensile Strength (MPa)
Young's modulus (GPa)
d
Immerse in water
20mm
Shape recovery
e
CCM
CCMA-1
CCMA-2
CCMA-3
Wet state
Tensile stress(MPa)
Tensile strain (%)
f
0 day
14 days
Stability of Covalent Networks
0 day
14 days
Tensile stress(MPa)
Tensile strain (%)
g
CCM
CCMA-1
CCMA-2
CCMA-3
CCM-cycle 5
CCMA-1-cycle 5
CCMA-2-cycle 5
CCMA-3-cycle 5
(R-direction)
Tensile stress (MPa)
Tensile strain (%)
h
Cycle 0
Cycle 5
Intensity (arb. units)
Φ = 0°
Φ (°)
i
Orientation factor
Cycles
j
Cycle 0
Cycle 5
Xc (%)
CCM
CCMA-1
CCMA-2
CCMA-3
k
Bulk Density (g·cm⁻³)
Resistance to shrinkage
Thickness (mm)
Cycles
l
Hydration
Dehydration
Scattered
Dense

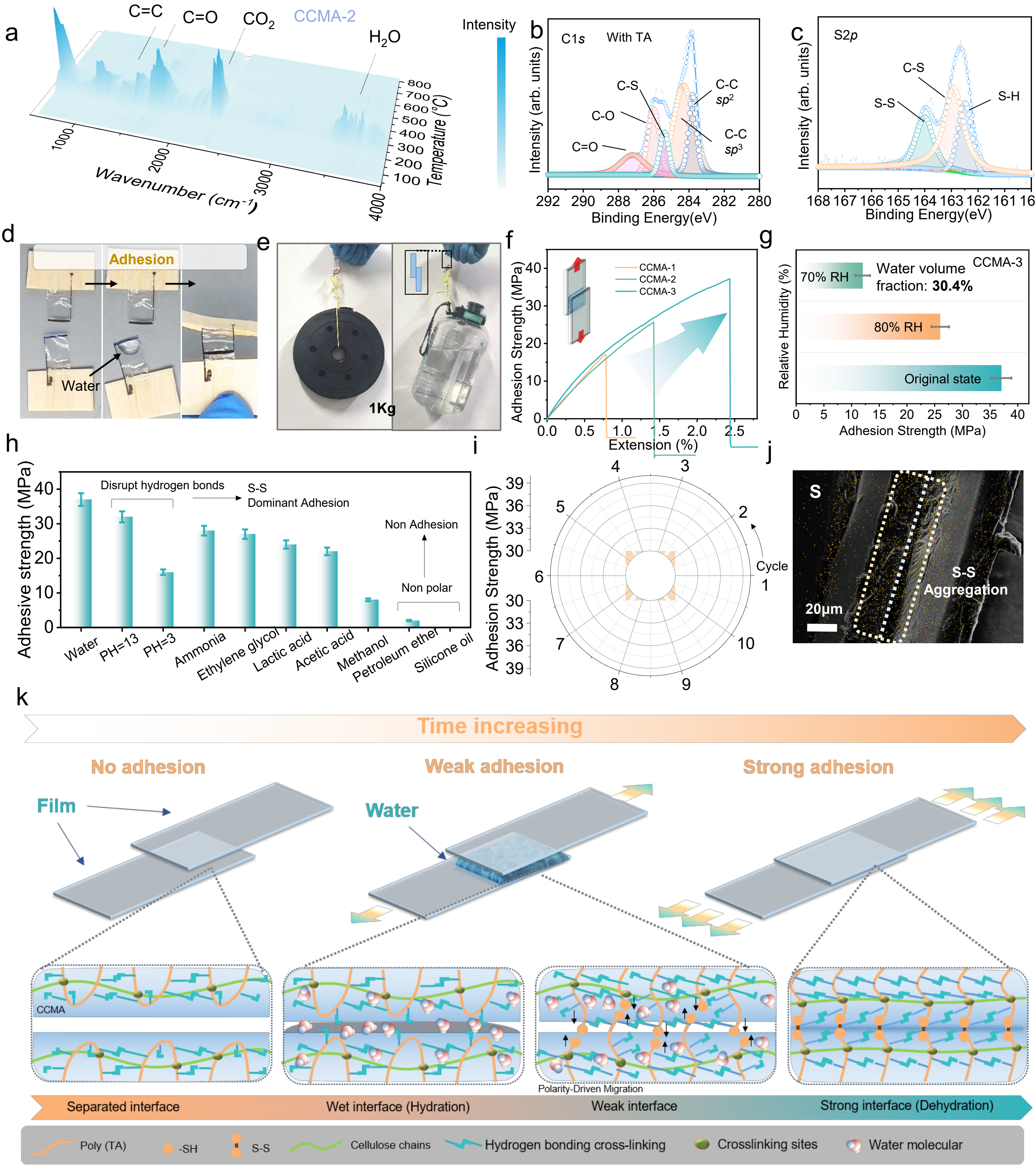
a
C=C
C=O
CO_2
CCMA-2
H_2O
Intensity
Wavenumber (cm⁻¹)
1000
2000
3000
4000
Temperature (°C)
100
200
300
400
500
600
700
800
b
C1s
With TA
C-S
C-O
C=O
C-C sp^2
C-C sp^3
Intensity (arb. units)
292 290 288 286 284 282 280
Binding Energy(eV)
c
S2p
C-S
S-S
S-H
Intensity (arb. units)
168 167 166 165 164 163 162 161 160
Binding Energy(eV)
d
Adhesion
Water
e
1Kg
f
CCMA-1
CCMA-2
CCMA-3
Adhesion Strength (MPa)
0 10 20 30 40
0.0 0.5 1.0 1.5 2.0 2.5
Extension (%)
g
CCMA-3
70% RH
Water volume fraction: **30.4%**
80% RH
Original state
Relative Humidity (%)
0 5 10 15 20 25 30 35 40
Adhesion Strength (MPa)
h
Disrupt hydrogen bonds
S-S Dominant Adhesion
Non Adhesion
Non polar
Adhesive strength (MPa)
0 10 20 30 40
Water
PH=13
PH=3
Ammonia
Ethylene glycol
Lactic acid
Acetic acid
Methanol
Petroleum ether
Silicone oil
i
Adhesion Strength (MPa)
39 36 33 30
30 33 36 39
1 2 3 4 5 6 7 8 9 10
Cycle
j
S
S-S Aggregation
20μm
k
Time increasing
No adhesion
Weak adhesion
Strong adhesion
Film
Water
CCMA
Polarity-Driven Migration
Separated interface
Wet interface (Hydration)
Weak interface
Strong interface (Dehydration)
Poly (TA)
-SH
S-S
Cellulose chains
Hydrogen bonding cross-linking
Crosslinking sites
Water molecular

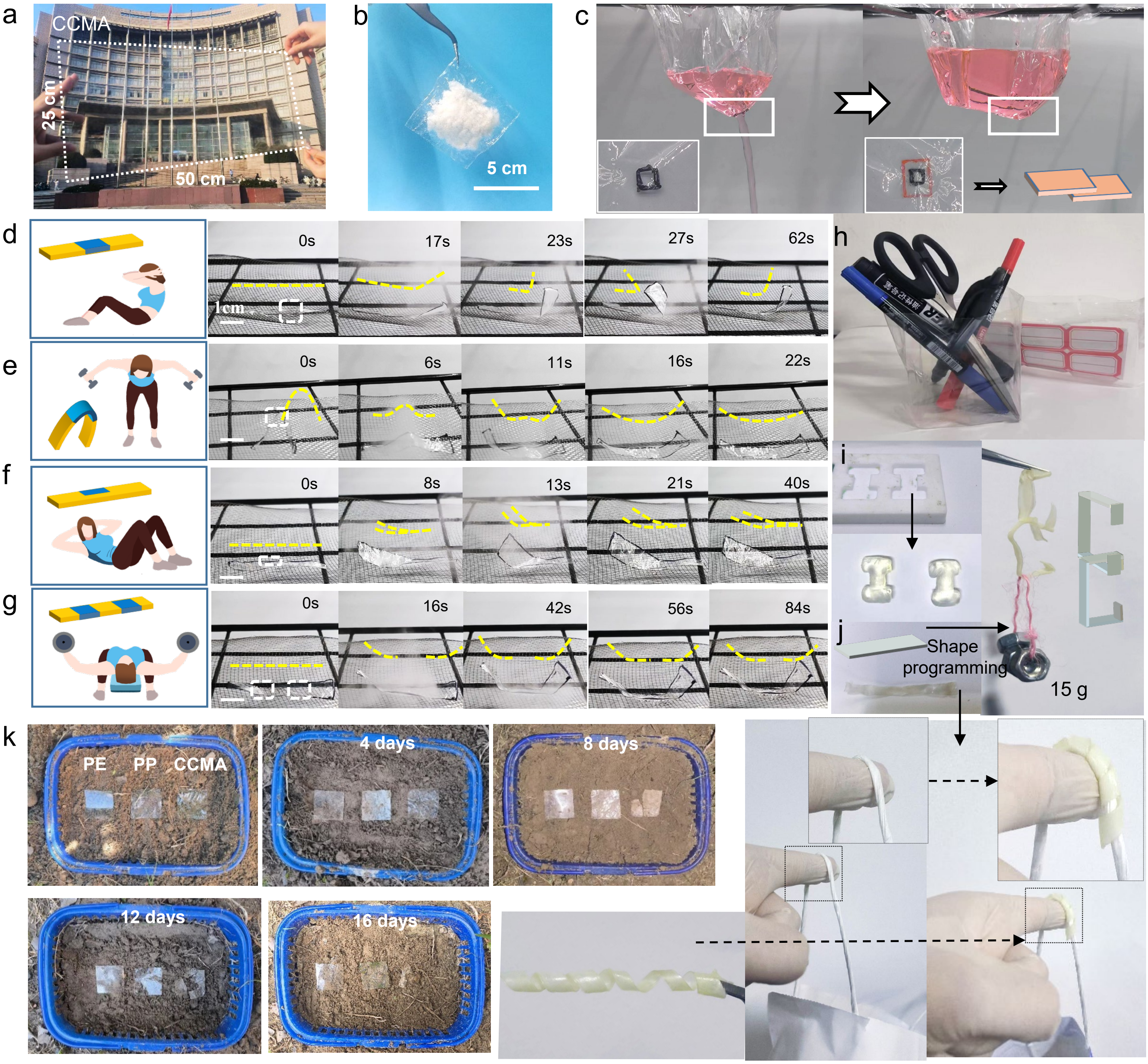
a
CCMA
25 cm
50 cm
b
5 cm
c
d
0s
17s
23s
27s
62s
1cm
e
0s
6s
11s
16s
22s
f
0s
8s
13s
21s
40s
g
0s
16s
42s
56s
84s
h
i
j
Shape
programming
15 g
k
PE
PP
CCMA
4 days
8 days
12 days
16 days